

See discussions, stats, and author profiles for this publication at: <https://www.researchgate.net/publication/233800795>

# XuCan2012

**DATASET** · DECEMBER 2012

---

READS

88

## 7 AUTHORS, INCLUDING:



[Haichun Liu](#)

Lund University

**26** PUBLICATIONS **393** CITATIONS

[SEE PROFILE](#)



[Maria E Messing](#)

Lund University

**62** PUBLICATIONS **1,084** CITATIONS

[SEE PROFILE](#)



[Can T Xu](#)

Lund University

**37** PUBLICATIONS **332** CITATIONS

[SEE PROFILE](#)



[Stefan andersson-engels](#)

Lund University

**326** PUBLICATIONS **6,134** CITATIONS

[SEE PROFILE](#)

# High-Resolution Fluorescence Diffuse Optical Tomography Developed with Nonlinear Upconverting Nanoparticles

Can T. Xu,<sup>†,\*</sup> Pontus Svenmarker,<sup>†</sup> Haichun Liu,<sup>†</sup> Xia Wu,<sup>†</sup> Maria E. Messing,<sup>‡</sup> L. Reine Wallenberg,<sup>§</sup> and Stefan Andersson-Engels<sup>†</sup>

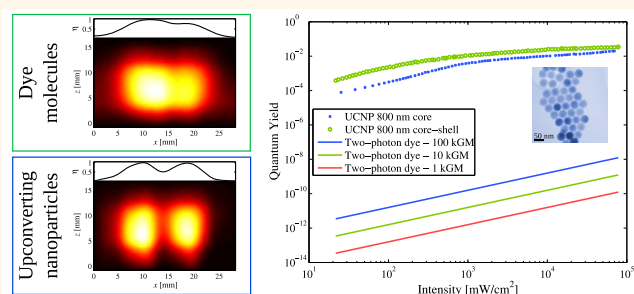
<sup>†</sup>Department of Physics, Lund University, Box 118, S-221 00 Lund, Sweden, <sup>‡</sup>Division of Solid State Physics, Lund University, Box 118, S-221 00 Lund, Sweden, and

<sup>§</sup>Polymer and Materials Chemistry/nCHREM, Lund University, Box 124, S-221 00 Lund, Sweden

Nanostructure contrast agents have become very important and versatile assets for optical imaging of biomedical systems. Nanostructures, such as quantum dots, carbon nanotubes, nanodiamonds, gold nanoparticles, and rare-earth-doped nanoparticles, have, for example, been explored for cancer targeting and treatment,<sup>1,2</sup> deep-tissue anatomical imaging of mice,<sup>3</sup> and background-free deep-tissue imaging of small animals.<sup>4–7</sup> For *in vivo* optical imaging of deeply situated fluorescent agents in biomedical systems, an emerging method of fluorescence diffuse optical tomography (FDOT) has recently been employed with an increasing interest.<sup>8–12</sup> FDOT is a compact, fast, and highly sensitive technique for three-dimensional deep-tissue imaging of fluorescent targets. These properties and the non-invasive nature of FDOT have made it very attractive for longitudinal studies of small animals, where it has been applied to follow the development in time of, for example, cancer tumors,<sup>13</sup> proteases,<sup>10</sup> Alzheimer's disease,<sup>14</sup> and different drug effects.<sup>12</sup>

Traditionally, the contrast agents used in FDOT are based on different types of Stokes-shifting fluorophores, such as molecular dyes or quantum dots. The linear power-density dependence of the emission from these fluorophores results in poor spatial resolution in the reconstructed images, as sharp spatial features are inevitably smeared out during diffuse light propagation. Several approaches have been employed to increase the spatial resolution, including multispectral methods,<sup>15</sup> the use of *a priori* information,<sup>16,17</sup> and structured illumination methods.<sup>18</sup> Although these approaches all have positive effects on the spatial resolution of the reconstructed images, ultimately they cannot circumvent the resolution-limiting factor originating

## ABSTRACT



Fluorescence diffuse optical tomography (FDOT) is an emerging biomedical imaging technique that can be used to localize and quantify deeply situated fluorescent molecules within tissues. However, the potential of this technique is currently limited by its poor spatial resolution. In this work, we demonstrate that the current resolution limit of FDOT can be breached by exploiting the nonlinear power-dependent optical emission property of upconverting nanoparticles doped with rare-earth elements. The rare-earth-doped core-shell nanoparticles, NaYF<sub>4</sub>:Yb<sup>3+</sup>/Tm<sup>3+</sup>@NaYF<sub>4</sub> of hexagonal phase, are synthesized through a stoichiometric method, and optical characterization shows that the upconverting emission of the nanoparticles in tissues depends quadratically on the power of excitation. In addition, quantum-yield measurements of the emission from the synthesized nanoparticles are performed over a large range of excitation intensities, for both core and core-shell particles. The measurements show that the quantum yield of the 800 nm emission band of core-shell upconverting nanoparticles is 3.5% under an excitation intensity of 78 W/cm<sup>2</sup>. The FDOT reconstruction experiments are carried out in a controlled environment using liquid tissue phantoms. The experiments show that the spatial resolution of the FDOT reconstruction images can be significantly improved by the use of the synthesized upconverting nanoparticles and break the current spatial resolution limits of FDOT images obtained from using conventional linear fluorophores as contrast agents.

**KEYWORDS:** upconversion nanoparticles · bioimaging · quantum yield · resolution · diffuse imaging

from the use of linear fluorophores in diffusive tissues. In this work, we report on the exploration of rare-earth-doped core-shell nanoparticles with upconverting optical properties as contrast agents for FDOT and demonstrate that the spatial resolution of FDOT can be significantly improved by exploiting their nonlinear power-dependent optical properties. The experiments were

\* Address correspondence to can.xu@fysik.lth.se.

Received for review December 19, 2011 and accepted May 7, 2012.

Published online May 08, 2012  
10.1021/nn3015807

© 2012 American Chemical Society

performed in a well-controlled environment using liquid tissue phantoms. Comparisons with FDOT reconstruction images obtained from an optically similar system employing linear fluorophores show that the spatial resolution of the reconstruction images obtained using the upconverting nanoparticles can go much beyond the current limits of conventional FDOT images. Using simulations, the mechanism behind the improved spatial resolution is described through a theoretical model. Furthermore, through careful optical characterization, we report, for the first time, the quantum yield of the 800 nm emission band and compare the quantum yield of core and core–shell particles. In addition to being a highly relevant material parameter, knowledge of the quantum yield enables the possibility to perform quantitative imaging of deeply situated targets within tissues.

Upconverting materials in bulk form have existed for decades.<sup>19</sup> However, only recently has it been possible to synthesize upconverting nanoparticles with quantum efficiencies high enough to be used as biological markers for microscopy and deep-tissue diffuse imaging.<sup>4,20–30</sup> Upconverting nanoparticles possess the unique property of being able to emit anti-Stokes-shifted light. This is accomplished by doping a host crystal with a sensitizer, typically  $\text{Yb}^{3+}$ , and an activator, for example,  $\text{Tm}^{3+}$ ,  $\text{Er}^{3+}$ , or  $\text{Ho}^{3+}$ . The sensitizer can, through mainly energy transfer upconversion, excite an activator in a stepwise manner, leading to the emission of anti-Stokes-shifted light.<sup>23,31,32</sup> This unique property has made upconverting nanoparticles very attractive for imaging and labeling of biological samples, yielding images that are virtually background free since the endogenous tissue autofluorescence is Stokes-shifted.<sup>4–6,28</sup> Furthermore, these particles are not susceptible to photobleaching and aging effects, in contrast to the commonly used dye molecules,<sup>27</sup> have a very low toxicity,<sup>33,34</sup> and can be used for multimodality imaging by carefully designing the synthesization process.<sup>35,36</sup> Recently, it has also been demonstrated that unwanted emission bands can be suppressed, which can be used for simplifying the instrumentation and enhancing the contrast.<sup>37</sup>

## RESULTS AND DISCUSSION

Core–shell  $\text{NaYF}_4:\text{Yb}^{3+}/\text{Tm}^{3+}@\text{NaYF}_4$  nanoparticles were utilized as contrast agents in this study. The core  $\text{NaYF}_4:\text{Yb}^{3+}/\text{Tm}^{3+}$  nanoparticles were synthesized through an efficient stoichiometric method,<sup>38</sup> and nonradiative losses caused by surface effects were reduced by coating the nanoparticles with an undoped layer of  $\text{NaYF}_4$ .<sup>28,39–41</sup> Due to the presence of the capping ligand (oleate), the  $\text{NaYF}_4:\text{Yb}^{3+}/\text{Tm}^{3+}@\text{NaYF}_4$  nanoparticles could be dispersed in nonpolar solvents and were colloidally stable for months without visible agglomeration. Figure 1a and b show transmission electron microscope (TEM) images of the synthesized

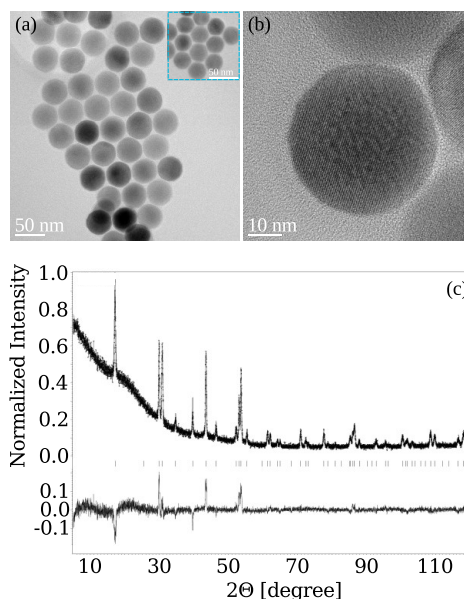


**Figure 1.** (a) TEM image of the monodisperse core–shell  $\text{NaYF}_4:\text{Yb}^{3+}/\text{Tm}^{3+}@\text{NaYF}_4$  nanoparticles. The inset shows the core  $\text{NaYF}_4:\text{Yb}^{3+}/\text{Tm}^{3+}$  nanoparticles prior to coating with the undoped  $\text{NaYF}_4$  layer. The mean diameters of the core–shell nanoparticles and the core nanoparticles were determined to be 43 and 31 nm, respectively. (b) High-resolution TEM image of the core–shell  $\text{NaYF}_4:\text{Yb}^{3+}/\text{Tm}^{3+}@\text{NaYF}_4$  nanoparticles. (c) XRD pattern of the synthesized core–shell  $\text{NaYF}_4:\text{Yb}^{3+}/\text{Tm}^{3+}@\text{NaYF}_4$  nanoparticles (top panel) and residual of fit for the hexagonal crystal phase (bottom panel).

core–shell  $\text{NaYF}_4:\text{Yb}^{3+}/\text{Tm}^{3+}@\text{NaYF}_4$  upconverting nanoparticles. The nanoparticles were spherical in shape with a mean diameter of 42 nm and had a dominant lattice spacing of 0.52 nm. The inset in Figure 1a shows the core nanoparticles, which through a comparison with the core–shell nanoparticles show that the thickness of the undoped  $\text{NaYF}_4$  shell was 6 nm. The X-ray diffraction (XRD) pattern of the synthesized core–shell  $\text{NaYF}_4:\text{Yb}^{3+}/\text{Tm}^{3+}@\text{NaYF}_4$  nanoparticles is shown in the top panel of Figure 1c with the residual of fit for the hexagonal crystal phase<sup>42</sup> shown in the bottom panel. The cell parameters of  $a = 5.976$  nm,  $b = 0.599$  nm, and  $c = 0.350$  nm are consistent with the pure hexagonal  $\text{NaYF}_4$  crystal in the JCPDS 16-0334 data.

Optical characterization of the synthesized core–shell nanoparticles was carried out using a spectrofluorometer setup under excitation by a laser diode at 975 nm. As shown in Figure 2, the excitation generated one strong emission band at 800 nm and two weak ones around 470 and 650 nm. These emission bands can be assigned to the transitions of  $\text{Tm}^{3+}$ .<sup>43</sup> The effective attenuation spectrum of a typical murine muscle tissue<sup>44</sup> is also presented in Figure 2, where it can be seen that light in the near-infrared region has considerably lower attenuation than light in the visible region. Thus, the emissions at the shorter wavelengths (470 and 650 nm) were filtered out and only the

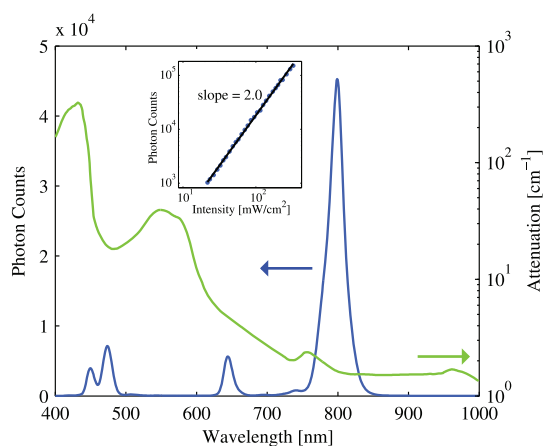


**Figure 2.** Emission spectrum (blue solid line) for the synthesized  $\text{NaYF}_4:\text{Yb}^{3+}/\text{Tm}^{3+}@\text{NaYF}_4$  nanoparticles of hexagonal phase under excitation at 975 nm and attenuation spectrum (green solid line) of typical murine muscle tissue. The excitation intensity was  $1 \text{ W}/\text{cm}^2$ , leading to a strong emission band at 800 nm. The weak emission bands around 470 and 650 nm are less suitable for use within tissues, since the attenuation at those wavelengths is significantly higher, as shown. The inset shows the power dependence of the emission band at 800 nm, demonstrating that the emission originates from a two-photon process.

emission at 800 nm was used for the experimental study in this work. The excitation at 975 nm and the emission at 800 nm are both highly suitable wavelengths residing around the optimal regions in the tissue optical window,<sup>44</sup> i.e., a region where tissue is relatively translucent and light penetration depths of several centimeters can be achieved. The inset in Figure 2 shows the power dependence of the 800 nm emission band of the nanoparticles. Since the fluence rate within scattering materials is in general small, the power dependence of the emission band was measured using weak excitation intensities, well below saturation limits.<sup>20</sup> From the slope of the linear fit (log–log scale), it can be seen that in contrast to the traditionally used fluorophores, which have a linear power dependence, the emission from the upconverting nanoparticles has a quadratic power dependence, consistent with the fact that the upconversion is a two-photon process.

The results from the quantum-yield measurements of both the synthesized core–shell and the core upconverting nanoparticles are shown in Figure 3. As seen, the synthesis produced efficient hexagonal core–shell  $\text{NaYF}_4:\text{Yb}^{3+}/\text{Tm}^{3+}@\text{NaYF}_4$  upconverting nanoparticles with a quantum yield of 3.5% under an excitation intensity of  $78 \text{ W}/\text{cm}^2$ . At the lower excitation intensity of  $21.7 \text{ mW}/\text{cm}^2$ , the quantum yield was determined to be  $3.8 \times 10^{-4}$ . Evidently, in this power-density regime, core–shell nanoparticles are, due to their protective shell layer, about 6 times brighter than unshielded particles.<sup>45</sup> Under low excitation intensities, the slope of the quantum yield is close to 1, consistent with the expected behavior for quadratic

fluorophores. As the excitation intensity is increased, the power dependence factor of the upconverting nanoparticles will begin to decrease due to saturation of the energy levels in the rare-earth ions,<sup>20</sup> resulting in a quantum yield that approaches a constant for large excitation intensities. For comparison, the quantum yields for the most efficient two-photon dyes were simulated under identical experimental conditions and are also shown in Figure 3. It can be seen that even for the very efficient dyes,<sup>46–48</sup> such as those based on fluorene derivatives,<sup>49,50</sup> the required excitation intensity is clearly too high to be used in scattering tissues. The reason is that these dyes require simultaneous absorption of two photons *via* a virtual state, in contrast to upconverting nanoparticles, which possess real long-lived intermediate states.

Reports on the absolute quantum yield of  $\text{NaYF}_4$  upconverting nanoparticles in the literature are very scarce.<sup>51–53</sup> For bulk  $\text{NaYF}_4:\text{Yb}^{3+}/\text{Tm}^{3+}$  material, Page *et al.*<sup>51</sup> have determined the power conversion factor of the blue emission band to be  $2 \times 10^{-4}$ , for the most efficient material studied at an excitation intensity of  $1 \text{ W}/\text{cm}^2$ . The corresponding power conversion factor for the synthesized core–shell  $\text{NaYF}_4:\text{Yb}^{3+}/\text{Tm}^{3+}@\text{NaYF}_4$  upconverting nanoparticles in this work was determined to be  $5.8 \times 10^{-5}$ . However, it is important to point out that since bulk material was used, direct comparisons with our results is nontrivial, without considering size-dependent effects. The size-dependent effects of  $\text{NaYF}_4:\text{Yb}^{3+}/\text{Er}^{3+}$  crystals have, however, been examined by Boyer *et al.*,<sup>53</sup> where a 10 times lower quantum yield of core–shell nanoparticles (30 nm) as compared with bulk material under an excitation intensity of  $150 \text{ W}/\text{cm}^2$  was found. Accounting for the size dependency, a more realistic power efficiency conversion factor that can be expected from the material used by Page *et al.*<sup>51</sup> should be  $2 \times 10^{-5}$ , which is in reasonable agreement with the results obtained in this work. However, as this is an indirect comparison, the results should be interpreted with caution and further studies of the efficiency of upconverting nanoparticles are certainly needed.

To evaluate the spatial resolution of FDOT with the use of the quadratically power-dependent upconverting nanoparticles and linearly power-dependent fluorophores as contrast agents, two 17 mm thick liquid phantoms consisting of water, intralipid, and ink were prepared. The concentrations of intralipid and ink were chosen to provide optical properties typically found in small animals.<sup>44</sup> Since the upconverting nanoparticles emit at 800 nm, DY-781 (Dyomics GmbH) dye molecules were chosen as the linear fluorophores, as they also emit at 800 nm. To further ensure a proper comparison between the FDOT images obtained using the linear fluorophores and the upconverting nanoparticles, the two phantoms were prepared to have identical optical properties at their respective excitation wavelengths of 785 and 975 nm. The phantom for

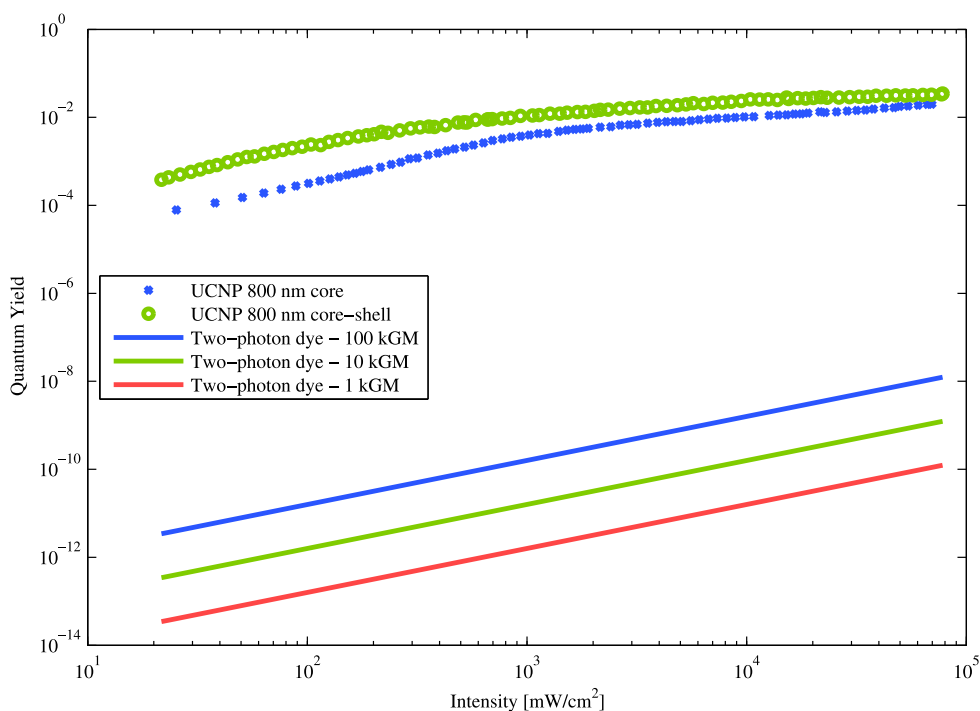


**Figure 3.** Quantum yield of the 800 nm emission band for the synthesized hexagonal core-shell  $\text{NaYF}_4:\text{Yb}^{3+}/\text{Tm}^{3+}@\text{NaYF}_4$  nanoparticles and hexagonal core  $\text{NaYF}_4:\text{Yb}^{3+}/\text{Tm}^{3+}$  nanoparticles. It can be seen that the quantum yield increases linearly (slope of 1) with the excitation intensity until a saturation point, from which the quantum yield approaches a constant value, which is the expected behavior for a linear fluorophore. Solid lines show simulated corresponding quantum yields for highly efficient two-photon dyes under identical experimental conditions, which in contrast to upconverting nanoparticles require two photons to be simultaneously absorbed. Compared with upconverting nanoparticles, even two-photon dyes with cross sections on the order of 100 kGM will be  $10^8$  times less bright.

the linear fluorophores had a reduced scattering coefficient of  $\mu'_s(785 \text{ nm}) = 10.1 \text{ cm}^{-1}$  and an absorption coefficient of  $\mu_a(785 \text{ nm}) = 0.51 \text{ cm}^{-1}$ , while the phantom for the upconverting nanoparticles had a reduced scattering coefficient of  $\mu'_s(975 \text{ nm}) = 10.1 \text{ cm}^{-1}$  and an absorption coefficient of  $\mu_a(975 \text{ nm}) = 0.52 \text{ cm}^{-1}$ , determined by a time-of-flight spectroscopy (TOFS) system.<sup>54</sup> The experimental setup is schematically illustrated in Figure 4, where two capillary tubes with inner diameters of 2.0 mm, filled with either the DY-781 fluorophores or the synthesized upconverting nanoparticles, were used to simulate fluorescent targets. By adjusting the center-to-center distance of the two fluorescent tubes and performing one tomographic reconstruction for each separation distance, the obtainable spatial resolution in the reconstruction images could be evaluated. It is important to note that autofluorescence can cause severe artifacts in the reconstructions for linear Stokes-shifting fluorophores.<sup>5</sup> Thus, a phantom material with low autofluorescence was selected, and any remaining autofluorescence effects or other background signals were removed by subtracting from each image its corresponding image obtained from a scan without any fluorescent targets.

Cross-sectional slices from the tomographic reconstructions for different center-to-center distances of the fluorescent tubes are shown in Figure 5. The reconstructions for the linearly power-dependent DY-781 fluorophores

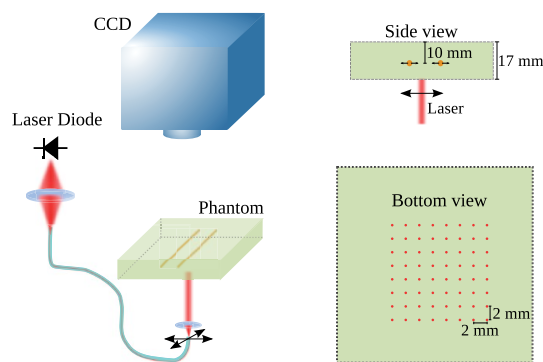


**Figure 4.** Schematic of the transilluminating experimental setup used for FDOT. An excitation beam was scanned from below in an  $8 \times 8$  grid pattern with each excitation spot separated from its neighbor spots by 2 mm (see the bottom view). A CCD camera was used to capture one image for each scanned position. Two fluorescent tubes, containing either the DY-781 fluorophores or the rare-earth-doped core-shell  $\text{NaYF}_4:\text{Yb}^{3+}/\text{Tm}^{3+}@\text{NaYF}_4$  upconverting nanoparticles, were mounted on a stage within the liquid phantom 10 mm from the top surface (see the side view). The separation distance between the two tubes was varied in discrete steps of 1 mm, and an FDOT reconstruction was performed for each separation distance.

are shown in Figure 5a to e, with decreasing tube separations from 10 mm in Figure 5a to 6 mm in Figure 5e. The corresponding reconstructions for the quadratically power-dependent  $\text{NaYF}_4:\text{Yb}^{3+}/\text{Tm}^{3+}@\text{NaYF}_4$  upconverting nanoparticles are shown in Figure 5f to m, with



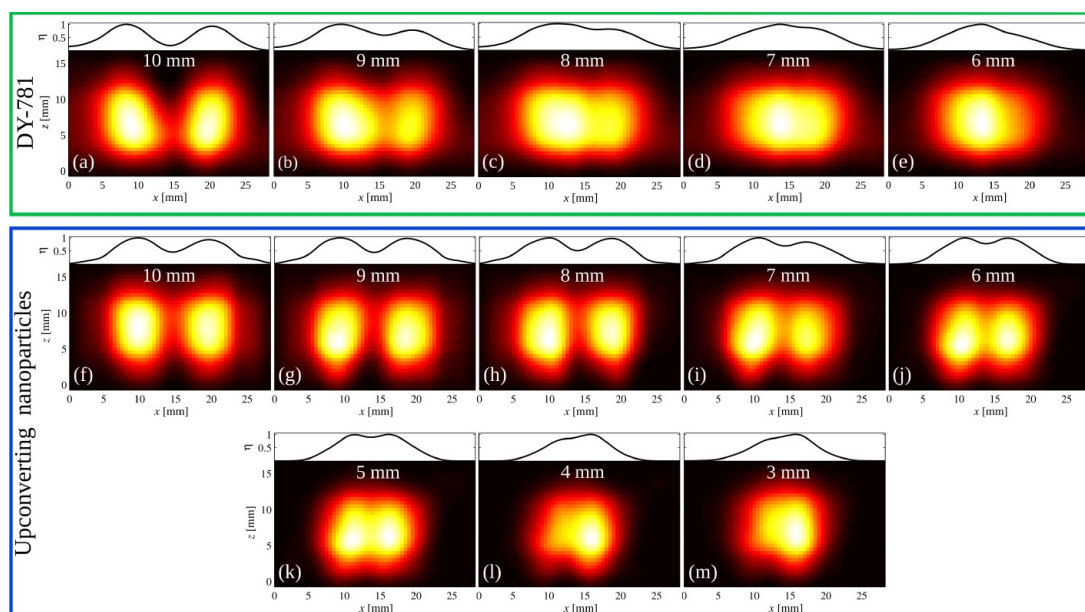


**Figure 5.** Cross-sectional slices (two-dimensional plots) of the FDOT reconstructions with the linearly power-dependent DY-781 fluorophores and the quadratically power-dependent  $\text{NaYF}_4:\text{Yb}^{3+}/\text{Tm}^{3+}@\text{NaYF}_4$  upconverting nanoparticles as contrast agents and their corresponding intensity profiles (line plots). The true depth was  $z = 7$  mm. The separation distance between the fluorescent tubes was varied from 10 to 6 mm (step sizes of 1 mm) for the case of the linear fluorophores, shown in (a)–(e). The use of quadratic upconverting nanoparticles clearly leads to reconstructions with higher spatial resolutions and qualities. Thus, the separation distance between the fluorescent tubes was varied from 10 to 3 mm (stepsizes of 1 mm), shown in (f)–(m). Using the linear fluorophores, already at a separation distance of 8 mm (c), the two fluorescent tubes can no longer be separated. However, in the images obtained with the use of the quadratic upconverting nanoparticles, besides the significantly higher qualities of the reconstructions, the two fluorescent tubes can still be separated at a separation distance of 5 mm (k).

decreasing tube separations, from 10 mm (Figure 5f) to 3 mm (Figure 5m). As can be seen, in all cases, the depth of the fluorescent tubes ( $z = 7$  mm) can be correctly retrieved. However, the difference in spatial resolution between the images with the use of the DY-781 fluorophores and the upconverting nanoparticles, in particular along the lateral dimension ( $x$ -axis), is immense. In the images obtained with the use of the upconverting nanoparticles, the two tubes can be retrieved from the reconstructions for separation distances down to 5 mm (Figure 5k). However, in the images obtained with the DY-781 fluorophores, retrieval of the two tubes breaks down already at 8 mm (Figure 5c). A comparison of the reconstructions in Figure 5h and c shows that the obtainable reconstruction quality by using the upconverting nanoparticles is exceedingly superior to what one could obtain with the use of traditional linear fluorophores. Furthermore, it is important to point out that although the optical properties of the phantom at the excitation wavelengths (785 and 975 nm) were chosen to be identical to ensure proper comparisons, this, inevitably resulted in slightly differing optical properties at the emission wavelength of 800 nm. Using TOFS, the optical properties of the phantom for the linear DY-781 fluorophores were determined to be  $\mu'_s(800 \text{ nm}) = 9.95 \text{ cm}^{-1}$  and  $\mu_a(800 \text{ nm}) = 0.49 \text{ cm}^{-1}$ , while the optical properties of the upconverting nanoparticles were  $\mu'_s(800 \text{ nm}) = 11.5 \text{ cm}^{-1}$  and  $\mu_a(800 \text{ nm}) = 0.041 \text{ cm}^{-1}$ . Thus, the

phantom for the upconverting nanoparticles, due to its higher scattering relative absorption ratio, is actually much more penalizing in terms of resolution as compared with the phantom for the DY-781 fluorophores.

The experimental results presented in this work clearly demonstrate that the spatial resolution of FDOT can be significantly improved by employing upconverting nanoparticles as contrast agents due to their nonlinear power-dependent optical properties. This improvement can be explained as follows by considering the effective light propagation profiles and the corresponding sensitivity profiles. For a given source–detector pair, the sensitivity profile describes the most probable origin of any detected emission light. Thus, a confined and sharp sensitivity profile results in a higher spatial resolution. Figure 6 shows simulated sensitivity profiles of traditionally used linear fluorophores and the quadratically power-dependent upconverting nanoparticles. The simulations were performed for three different source positions, with the detector position fixed. The circles within the slices indicate the positions of two fluorescent tubes separated by 5 mm. Comparing the sensitivity profiles of the linear fluorophores (Figure 6a–c) and the sensitivity profiles of the quadratically power-dependent upconverting nanoparticles (Figure 6d–f), it is evident that the gradient for the quadratic case, in particular close to the source, is much larger than

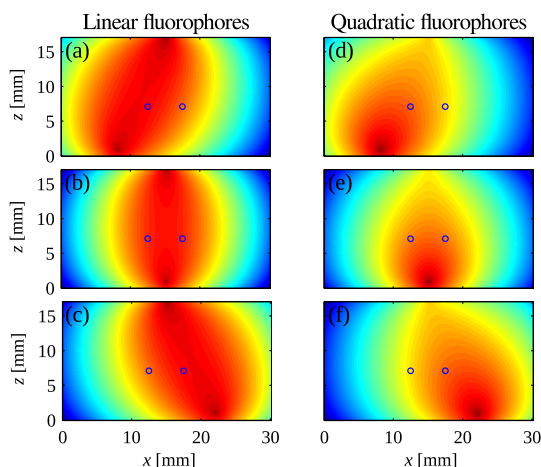


**Figure 6.** Simulated sensitivity profiles of linearly power-dependent fluorophores and quadratically power-dependent upconverting nanoparticles for three source positions and a fixed detector position. The circles represent the experimental case of two fluorescent tubes with a center-to-center separation of 5 mm. (a–c) Sensitivity profiles of linear fluorophores. (d–f) Sensitivity profiles of the upconverting nanoparticles. From the figure, it is clear that the quadratic power dependence of the emission results in sensitivity profiles that are much more confined and sharply defined as compared with linear fluorophores. Thus, the two fluorescent targets can effectively be selectively excited if upconverting nanoparticles are employed as contrast agents.

the gradient for the linear case. Therefore, here selective excitation of the individual fluorescent targets can be achieved if upconverting nanoparticles are employed. The large excitation volumes resulting from employing traditional linear fluorophores, on the other hand, severely limit the spatial selectivity.

The resolution in the lateral dimension was experimentally investigated in this study. However, since the resolution enhancement originates from the confinement of the sensitivity profile for the upconverting nanoparticles, it is clear that the axial resolution will certainly also exhibit a higher spatial resolution as compared with linear fluorophores. This intrinsic property of

nonlinear upconverting nanoparticles that leads to selective excitation should be applicable to arbitrary geometries and will in all cases excel linear fluorophores in terms of spatial resolution. Furthermore, since the resolution enhancement can be attributed to an intrinsic property of the upconverting nanoparticles, it is possible and straightforward to implement the previously mentioned approaches, such as multi-spectral methods, incorporation of *a priori* information, and other mathematical formulations of the problem, to further improve the spatial resolution.

## CONCLUSIONS

In summary, core–shell  $\text{NaYF}_4:\text{Yb}^{3+}/\text{Tm}^{3+}@\text{NaYF}_4$  upconverting nanoparticles of hexagonal phase have been synthesized and employed as contrast agents in the demonstration of FDOT with high spatial resolution. The optical characterization shows that the emission from the core–shell nanoparticles depends quadratically on the power of excitation in tissues and that the quantum yield of the synthesized upconverting nanoparticles is 3.5% under a more intense excitation intensity of  $78 \text{ W/cm}^2$ . It is demonstrated that the spatial resolution of FDOT can be significantly improved by exploiting the nonlinear optical emission properties of the upconverting core–shell nanoparticles as compared with the traditionally used fluorophores. In contrast to previously employed approaches to improve the spatial resolution of FDOT, which mainly aim to utilize and optimize the available data, our approach attacks the limiting factor directly by instead tailoring the shape of the sensitivity profiles. This fundamentally different approach, which exploits the unique nonlinear power-dependent emission property of upconverting nanoparticles, significantly improves the current spatial-resolution limit of FDOT, enabling deep-tissue optical imaging of targets in biomedical systems with unprecedented resolutions.

## EXPERIMENTAL METHODS

**Synthesis and Characterization of the Nanoparticles.** In the synthesis of the core  $\text{NaYF}_4:\text{Yb}^{3+}/\text{Tm}^{3+}$  nanoparticles, stoichiometric amounts of  $\text{YCl}_3$  (0.75 mmol),  $\text{YbCl}_3$  (0.25 mmol), and  $\text{TmCl}_3$  (0.003 mmol) were mixed with 6 mL of oleic acid (OA) and 17 mL of octadecene (ODE) in a 250 mL flask. The mixture was heated to  $160^\circ\text{C}$  for 30 min, forming a clear solution. Then, 4 mmol of  $\text{NH}_4\text{F}$  (0.1482 g) and 2.5 mmol of  $\text{NaOH}$  (0.1 g) dissolved in 10 mL of methanol was aspirated into a syringe and added into the solution by a syringe pump using a flow rate of 200 L/min. The obtained solution was first slowly heated to evaporate the methanol and degassed at  $100^\circ\text{C}$  for 10 min, followed by a second step of heating to  $300^\circ\text{C}$  for 1.5 h under an argon atmosphere. After the solution had cooled to room temperature, the nanoparticles were precipitated and washed with 100 mL of ethanol/water mixture (1:1 v/v) three times and centrifuged at 5100 rpm for 10 min before being collected and redispersed in 6 mL of *n*-hexane. In order to reduce the nonradiative losses caused by surface effects, the nanoparticles

were further coated with an undoped layer of  $\text{NaYF}_4$  through a similar procedure to that above. A clear solution containing 1.00 mmol of  $\text{Y}^{3+}$  was first obtained by dissolving  $\text{YCl}_3$  in 6 mL of oleic acid and 17 mL of ODE in a 200 mL flask.  $\text{NaYF}_4:\text{Yb}^{3+}/\text{Tm}^{3+}$  nanoparticles (1 mmol) in 6 mL of hexane was then added to the solution. Using a syringe pump, with the above-mentioned flow rate, 4 mmol of  $\text{NH}_4\text{F}$  (0.1482 g) and 2.5 mmol of  $\text{NaOH}$  (0.1 g) in 10 mL of methanol was added. The following steps, including degassing, reaction, precipitation, washing, centrifugation, and collection, were identical to the synthesis of the core nanoparticles. TEM images were obtained using a JEOL 3000F analytical transmission electron microscope.

Optical characterization of the core–shell nanoparticles was performed using a sensitive spectrofluorometer setup. Excitation of the synthesized core–shell nanoparticles was performed using the Thorlabs L975P1WJ laser diode with the temperature stabilized at  $25^\circ\text{C}$ . The emission was measured using a grating spectrometer with a slit width of 50 m (Ocean Optics QE65000). For the quantum-yield measurements, the system employed

standard fluorophores calibrated using the integrating-sphere-based Hamamatsu C9920 quantum yield measurement system. The resulting quantum yield of the upconverting nanoparticles was thus given by

$$\Phi_{\text{NP}} = \frac{A_s}{A_{\text{NP}}} \frac{F_{\text{NP}}}{F_s} \Phi_s \quad (1)$$

where  $A$  denotes the fraction of absorbed photons,  $\Phi$  is the quantum yield,  $F$  is the collected photons, and the subscripts  $s$  and  $\text{NP}$  denote the standard and the upconverting nanoparticles, respectively.

**FDOT Imaging System.** Imaging of the phantom was performed in a transmission mode. Four capillary tubes with inner diameters of 2.0 mm were used to simulate fluorescent targets. The first two tubes were filled with a solution of DY-781 ( $c = 1 \mu\text{M}$ ), and the last two tubes were filled with a solution of the  $\text{NaYF}_4:\text{Yb}^{3+}/\text{Tm}^{3+}@\text{NaYF}_4$  nanoparticles ( $c = 1 \text{ wt } \%$ ). For each type of fluorophores, two tubes were mounted in parallel (in the lateral direction) on a 7 mm tall stage immersed within the tissue phantom. The center-to-center distance of the two tubes had an initial value of 10 mm and was gradually decreased with a step size of 1 mm. A tomographic reconstruction was performed for each separation distance. Excitation of the fluorophores was accomplished using a laser diode at 785 nm for the linear fluorophores and at 975 nm for the upconverting nanoparticles, illuminating the phantom from below with spot sizes of 1 mm. The excitation intensities at the surface of the phantoms were moderate ( $95 \text{ mW}/\text{cm}^2$  for the 785 nm laser and  $800 \text{ mW}/\text{cm}^2$  for the 975 nm laser), well below the thresholds for tissue damage. For each reconstruction, the excitation beam was scanned over an area of  $14 \times 14 \text{ mm}^2$  in an  $8 \times 8$  grid using two computer-controlled translation stages. A charge-coupled device (CCD) camera (Andor iXon) was used to acquire one image for every scanned position. After background and autofluorescence subtraction, the signal-to-noise ratios of the resulting images for the DY-781 fluorophores and the upconverting nanoparticles were very similar and were determined to be 52:1 for the DY-781 fluorophores and 62:1 for the upconverting nanoparticles.

**FDOT Model.** The FDOT technique is a model-based inverse approach that aims to find the fluorophore or the nanoparticle number density,  $\eta(\mathbf{r})$ , within a scattering material. Using a set of fluence measurements on the surface of the media and a forward model, the problem was formulated as an optimization problem where  $\eta$  is optimized to minimize the residual between a predicted set of measurement data,  $\Theta_f^p(\eta)$ , and a set of experimentally retrieved measurement data,  $\Theta_f^m$ . In this study, the excitation field,  $\Phi_e(\mathbf{r})$ , and the emission field,  $\Phi_f(\mathbf{r})$ , were modeled using two coupled diffusion equations,

$$(\mu_a^e - \kappa_e(\mathbf{r})\nabla^2)\Phi_e(\mathbf{r}) = S(\mathbf{r}) \quad (2)$$

$$(\mu_a^f - \kappa_f(\mathbf{r})\nabla^2)\Phi_f(\mathbf{r}) = \xi\eta(\mathbf{r})\Phi_e^\gamma(\mathbf{r}) \quad (3)$$

where  $\xi$  is a constant denoting the efficiency of a fluorophore and  $\gamma$  describes the power dependence of a fluorophore, i.e.,  $\gamma = 1$  for a linear fluorophore and  $\gamma = 2$  for a quadratic fluorophore such as the upconverting nanoparticles employed in this study;  $\mu_a^{e,f}$  and  $\kappa_{e,f}$  denote the absorption and diffusion coefficient at the excitation and fluorescence wavelengths, respectively. The diffusion equations were solved using the finite-element method, and Robin boundary conditions were used to account for the refractive index mismatch between the phantom material and the surrounding air. Since the problem is highly ill-posed, Tikhonov regularization was used in the optimization process to obtain a stable solution, and the regularization parameter was derived by gradually decreasing an initially large value, until a plateau in the residual was reached.<sup>5</sup>

**Conflict of Interest:** The authors declare no competing financial interest.

**Acknowledgment.** E. Alerstam is gratefully acknowledged for the help with the TOFS measurements. S. Lidin and C. Müller are acknowledged for the help with the XRD measurements.

S. Fredriksson and F. Olsson are acknowledged for the help with synthesizing the nanoparticles. This work was supported by grants from the Swedish Research Council, the Crafoord Foundation, a Linnaeus grant to the Lund Laser Centre, and a Linnaeus grant for Nanoscience and Quantum Engineering.

## REFERENCES AND NOTES

- Gao, X.; Cui, Y.; Levenson, R. M.; Chung, L. W. K.; Nie, S. *In Vivo* Cancer Targeting and Imaging with Semiconductor Quantum Dots. *Nat. Biotechnol.* **2004**, *22*, 969–976.
- Huang, X. H.; Neretina, S.; El-Sayed, M. A. Gold Nanorods: From Synthesis and Properties to Biological and Biomedical Applications. *Adv. Mater.* **2009**, *21*, 4880–4910.
- Welsher, K.; Sherlock, S. P.; Dai, H. J. Deep-Tissue Anatomical Imaging of Mice Using Carbon Nanotube Fluorophores in the Second Near-Infrared Window. *Proc. Natl. Acad. Sci. U. S. A.* **2011**, *108*, 8943–8948.
- Chatterjee, D. K.; Rufalnah, A. J.; Zhang, Y. Upconversion Fluorescence Imaging of Cells and Small Animals Using Lanthanide Doped Nanocrystals. *Biomaterials* **2008**, *29*, 937–943.
- Xu, C. T.; Axelsson, J.; Andersson-Engels, S. Fluorescence Diffuse Optical Tomography Using Upconverting Nanoparticles. *Appl. Phys. Lett.* **2009**, *94*, 251107.
- Xu, C. T.; Svensson, N.; Axelsson, J.; Svenmarker, P.; Somesfalean, G.; Chen, G.; Liang, H.; Liu, H.; Zhang, Z.; Andersson-Engels, S. Autofluorescence Insensitive Imaging Using Upconverting Nanocrystals in Scattering Media. *Appl. Phys. Lett.* **2008**, *93*, 171103.
- Zhan, Q.; Qian, J.; Liang, H.; Somesfalean, G.; Wang, D.; He, S.; Zhang, Z.; Andersson-Engels, S. Using 915 nm Laser Excited  $\text{Tm}^{3+}/\text{Er}^{3+}/\text{Ho}^{3+}$ -Doped  $\text{NaYF}_4$  Upconversion Nanoparticles for *in Vitro* and Deeper *in Vivo* Bioimaging without Overheating Irradiation. *ACS Nano* **2011**, *5*, 3744–3757.
- Ntziachristos, V.; Ripoll, J.; Wang, L. H. V.; Weissleder, R. Looking and Listening to Light: The Evolution of Whole-Body Photonic Imaging. *Nat. Biotechnol.* **2005**, *23*, 313–320.
- Hielscher, A. H. Optical Tomographic Imaging of Small Animals. *Curr. Opin. Biotechnol.* **2005**, *16*, 79–88.
- Ntziachristos, V.; Tung, C.-H.; Bremer, C.; Weissleder, R. Fluorescence Molecular Tomography Resolves Protease Activity *in Vivo*. *Nat. Med. (N. Y., NY, U. S.)* **2002**, *8*, 757–760.
- Ntziachristos, V. Going Deeper than Microscopy: The Optical Imaging Frontier in Biology. *Nat. Methods* **2010**, *7*, 603–614.
- Ntziachristos, V.; Schellenberger, E.; Ripoll, J.; Yessayan, D.; Graves, E.; Bogdanov, A.; Josephson, L.; Weissleder, R. Visualization of Antitumor Treatment by Means of Fluorescence Molecular Tomography with an Annexin V-Cy5.5 Conjugate. *Proc. Natl. Acad. Sci. U. S. A.* **2004**, *101*, 12294–12299.
- Corlu, A.; Choe, R.; Durduran, T.; Rosen, M. A.; Schweiger, M.; Arridge, S. R.; Schnall, M. D.; Yodh, A. G. Three-Dimensional *in Vivo* Fluorescence Diffuse Optical Tomography of Breast Cancer in Humans. *Opt. Express* **2007**, *15*, 6696–6716.
- Hyde, D.; de Kleine, R.; MacLaurin, S. A.; Miller, E.; Brooks, D. H.; Krucker, T.; Ntziachristos, V. Hybrid FMT-CT Imaging of Amyloid-Beta Plaques in a Murine Alzheimer's Disease Model. *Neuroimage* **2009**, *44*, 1304–1311.
- Chaudhari, A. J.; Ahn, S.; Levenson, R.; Badawi, R. D.; Cherry, S. R.; Leahy, R. M. Excitation Spectroscopy in Multispectral Optical Fluorescence Tomography: Methodology, Feasibility and Computer Simulation Studies. *Phys. Med. Biol.* **2009**, *54*, 4687–4704.
- Lin, Y. T.; Yan, H.; Nalciglu, O.; Gulsen, G. Quantitative Fluorescence Tomography with Functional and Structural a Priori Information. *Appl. Opt.* **2009**, *48*, 1328–1336.
- Panagiotou, C.; Somayajula, S.; Gibson, A. P.; Schweiger, M.; Leahy, R. M.; Arridge, S. R. Information Theoretic Regularization in Diffuse Optical Tomography. *J. Opt. Soc. Am. A* **2009**, *26*, 1277–1290.



18. Mazhar, A.; Cuccia, D. J.; Gioux, S.; Durkin, A. J.; Frangioni, J. V.; Tromberg, B. J. Structured Illumination Enhances Resolution and Contrast in Thick Tissue Fluorescence Imaging. *J. Biomed. Opt.* **2010**, *15*, 010506.
19. Menyuk, N.; Pierce, J.; Dwight, K. NaYF<sub>4</sub>:Yb,Er - Efficient Upconversion Phosphor. *Appl. Phys. Lett.* **1972**, *21*, 159–161.
20. Haase, M.; Schafer, H. Upconverting Nanoparticles. *Angew. Chem., Int. Ed.* **2011**, *50*, 5808–5829.
21. Mader, H. S.; Kele, P.; Saleh, S. M.; Wolfbeis, O. S. Upconverting Luminescent Nanoparticles for Use in Bioconjugation and Bioimaging. *Curr. Opin. Chem. Biol.* **2010**, *14*, 582–596.
22. Ong, L. C.; Gnanasamandhan, M. K.; Nagarajan, S.; Zhang, Y. Upconversion: Road to El Dorado of the Fluorescence World. *Luminescence* **2010**, *25*, 290–293.
23. Wang, F.; Banerjee, D.; Liu, Y. S.; Chen, X. Y.; Liu, X. G. Upconversion Nanoparticles in Biological Labeling, Imaging, and Therapy. *Analyst (Cambridge, U. K.)* **2010**, *135*, 1839–1854.
24. Liu, H. C.; Xu, C. T.; Andersson-Engels, S. Multibeam Fluorescence Diffuse Optical Tomography Using Upconverting Nanoparticles. *Opt. Lett.* **2010**, *35*, 718–720.
25. Svenmarker, P.; Xu, C. T.; Andersson-Engels, S. Use of Nonlinear Upconverting Nanoparticles Provides Increased Spatial Resolution in Fluorescence Diffuse Imaging. *Opt. Lett.* **2010**, *35*, 2789–2791.
26. Nyk, M.; Kumar, R.; Ohulchanskyy, T. Y.; Bergey, E. J.; Prasad, P. N. High Contrast *in Vitro* and *in Vivo* Photoluminescence Bioimaging Using Near Infrared to Near Infrared Up-Conversion in Tm<sup>3+</sup> and Yb<sup>3+</sup> Doped Fluoride Nanophosphors. *Nano Lett.* **2008**, *8*, 3834–3838.
27. Bouzigues, C.; Gacoin, T.; Alexandrou, A. Biological Applications of Rare-Earth Based Nanoparticles. *ACS Nano* **2011**, *5*, 8488–8505.
28. Wang, F.; Deng, R. R.; Wang, J.; Wang, Q. X.; Han, Y.; Zhu, H. M.; Chen, X. Y.; Liu, X. G. Tuning Upconversion through Energy Migration in Core-Shell Nanoparticles. *Nat. Mater.* **2011**, *10*, 968–973.
29. Cao, T. Y.; Yang, Y.; Gao, Y. A.; Zhou, J.; Li, Z. Q.; Li, F. Y. High-Quality Water-Soluble and Surface-Functionalized Upconversion Nanocrystals as Luminescent Probes for Bioimaging. *Biomaterials* **2011**, *32*, 2959–2968.
30. Bunzli, J. C. G. Lanthanide Luminescence for Biomedical Analyses and Imaging. *Chem. Rev. (Washington, DC, U. S.)* **2010**, *110*, 2729–2755.
31. Auzel, F. Upconversion and Anti-Stokes Processes with f and d Ions in Solids. *Chem. Rev. (Washington, DC, U. S.)* **2004**, *104*, 139–173.
32. Yi, G.; Lu, H.; Zhao, S.; Yue, G.; Yang, W.; Chen, D.; Guo, L. Synthesis, Characterization, and Biological Application of Size-Controlled Nanocrystalline NaYF<sub>4</sub>:Yb,Er Infrared-to-Visible Up-Conversion Phosphors. *Nano Lett.* **2004**, *4*, 2191–2196.
33. Lim, S. F.; Riehn, R.; Tung, C. K.; Ryu, W. S.; Zhuo, R.; Dalland, J.; Austin, R. H. Upconverting Nanophosphors for Bioimaging. *Nanotechnology* **2009**, *20*, 405701.
34. Nam, S. H.; Bae, Y. M.; Il Park, Y.; Kim, J. H.; Kim, H. M.; Choi, J. S.; Lee, K. T.; Hyeon, T.; Suh, Y. D. Long-Term Real-Time Tracking of Lanthanide Ion Doped Upconverting Nanoparticles in Living Cells. *Angew. Chem., Int. Ed.* **2011**, *50*, 6093–6097.
35. Zhou, J.; Yu, M. X.; Sun, Y.; Zhang, X. Z.; Zhu, X. J.; Wu, Z. H.; Wu, D. M.; Li, F. Y. Fluorine-18-Labeled Gd<sup>3+</sup>/Yb<sup>3+</sup>/Er<sup>3+</sup> Co-Doped NaYF<sub>4</sub> Nanophosphors for Multimodality PET/MR/UCL Imaging. *Biomaterials* **2011**, *32*, 1148–1156.
36. Liu, Q.; Chen, M.; Sun, Y.; Chen, G. Y.; Yang, T. S.; Gao, Y.; Zhang, X. Z.; Li, F. Y. Multifunctional Rare-Earth Self-Assembled Nanosystem for Tri-Modal Upconversion Luminescence/Fluorescence/Positron Emission Tomography Imaging. *Biomaterials* **2011**, *32*, 8243–8253.
37. Wang, J.; Wang, F.; Wang, C.; Liu, Z.; Liu, X. G. Single-Band Upconversion Emission in Lanthanide-Doped KMnF<sub>3</sub> Nanocrystals. *Angew. Chem., Int. Ed.* **2011**, *50*, 10369–10372.
38. Li, Z. Q.; Zhang, Y. An Efficient and User-Friendly Method for the Synthesis of Hexagonal-Phase NaYF<sub>4</sub>:Yb, Er/Tm Nanocrystals with Controllable Shape and Upconversion Fluorescence. *Nanotechnology* **2008**, *19*, 345606.
39. Boyer, J.; Vetrone, F.; Cuccia, L.; Capobianco, J. Synthesis of Colloidal Upconverting NaYF<sub>4</sub> Nanocrystals Doped with Er<sup>3+</sup>, Yb<sup>3+</sup> and Tm<sup>3+</sup>, Yb<sup>3+</sup> via Thermal Decomposition of Lanthanide Trifluoroacetate Precursors. *J. Am. Chem. Soc.* **2006**, *128*, 7444–7445.
40. Qian, H. S.; Zhang, Y. Synthesis of Hexagonal-Phase Core-Shell NaYF<sub>4</sub> Nanocrystals with Tunable Upconversion Fluorescence. *Langmuir* **2008**, *24*, 12123–12125.
41. Ow, H.; Larson, D. R.; Srivastava, M.; Baird, B. A.; Webb, W. W.; Wiesner, U. Bright and Stable Core-Shell Fluorescent Silica Nanoparticles. *Nano Lett.* **2005**, *5*, 113–117.
42. Wang, Z. J.; Tao, F.; Yao, L. Z.; Cai, W. L.; Li, X. G. Selected Synthesis of Cubic and Hexagonal NaYF<sub>4</sub> Crystals via a Complex-Assisted Hydrothermal Route. *J. Cryst. Growth* **2006**, *290*, 296–300.
43. Wei, Y.; Lu, F. Q.; Zhang, X. R.; Chen, D. P. Synthesis and Characterization of Efficient Near-Infrared Upconversion Yb and Tm Codoped NaYF<sub>4</sub> Nanocrystal Reporter. *J. Alloys Compd.* **2007**, *427*, 333–340.
44. Alexandrakis, G.; Rannou, F. R.; Chatziioannou, A. F. Tomographic Bioluminescence Imaging by Use of a Combined Optical-PET (OPET) System: A Computer Simulation Feasibility Study. *Phys. Med. Biol.* **2005**, *50*, 4225–4241.
45. Wang, F.; Wang, J. A.; Liu, X. G. Direct Evidence of a Surface Quenching Effect on Size-Dependent Luminescence of Upconversion Nanoparticles. *Angew. Chem., Int. Ed.* **2010**, *49*, 7456–7460.
46. He, G. S.; Bhawalkar, J. D.; Zhao, C. F.; Prasad, P. N. Optical Limiting Effect In a 2-photon Absorption Dye-Doped Solid-matrix. *Appl. Phys. Lett.* **1995**, *67*, 2433–2435.
47. Pawlicki, M.; Collins, H. A.; Denning, R. G.; Anderson, H. L. Two-Photon Absorption and the Design of Two-Photon Dyes. *Angew. Chem., Int. Ed.* **2009**, *48*, 3244–3266.
48. Drobizhev, M.; Makarov, N. S.; Tillo, S. E.; Hughes, T. E.; Rebane, A. Two-Photon Absorption Properties of Fluorescent Proteins. *Nat. Methods* **2011**, *8*, 393–399.
49. Belfield, K. D.; Morales, A. R.; Kang, B. S.; Hales, J. M.; Hagan, D. J.; Van Stryland, E. W.; Chapela, V. M.; Percino, J. Synthesis, Characterization, and Optical Properties of New Two-Photon-Absorbing Fluorene Derivatives. *Chem. Mater.* **2004**, *16*, 4634–4641.
50. Reinhardt, B. A.; Brott, L. L.; Clarson, S. J.; Dillard, A. G.; Bhatt, J. C.; Kannan, R.; Yuan, L.; He, G. S.; Prasad, P. N. Highly Active Two-Photon Dyes: Design, Synthesis, and Characterization toward Application. *Chem. Mater.* **1998**, *10*, 1863–1874.
51. Page, R. H.; Schaffers, K. I.; Waide, P. A.; Tassano, J. B.; Payne, S. A.; Krupke, W. F.; Bischel, W. K. Upconversion-Pumped Luminescence Efficiency of Rare-Earth-Doped Hosts Sensitized with Trivalent Ytterbium. *J. Opt. Soc. Am. B* **1998**, *15*, 996–1008.
52. Suyver, J.; Grimm, J.; van Veen, M.; Biner, D.; Kramer, K.; Gudiel, H. Upconversion Spectroscopy and Properties of NaYF<sub>4</sub> Doped with Er<sup>3+</sup>, Tm<sup>3+</sup> and/or Yb<sup>3+</sup>. *J. Lumin.* **2006**, *117*, 1–12.
53. Boyer, J. C.; van Veggel, F. C. J. M. Absolute Quantum Yield Measurements of Colloidal NaYF<sub>4</sub>:Er<sup>3+</sup>, Yb<sup>3+</sup> Upconverting Nanoparticles. *Nanoscale* **2010**, *2*, 1417–1419.
54. Svensson, T.; Alerstam, E.; Khoptyar, D.; Johansson, J.; Folestad, S.; Andersson-Engels, S. Near-Infrared Photon Time-of-Flight Spectroscopy of Turbid Materials up to 1400 nm. *Rev. Sci. Instrum.* **2009**, *80*, 063105.